

Ultraquantum magnetoresistance in single-crystalline β -Ag₂Se

Chenglong Zhang^{1†}, Haiwen Liu^{1†}, Tay-Rong Chang³, Su-Yang

Xu⁴, Wei Hua⁵, Hua Jiang⁶, Zhujun Yuan¹, Junliang Sun⁵,

Horng-Tay Jeng^{3,7}, M. Zahid Hasan⁴, X.C. Xie^{1,2}, Shuang Jia^{1,2*}

¹*ICQM, School of Physics, Peking University, Beijing 100871, China*

²*Collaborative Innovation Center of Quantum Matter, Beijing, China*

³*Department of Physics, National Tsing Hua University, Hsinchu 30013, Taiwan*

⁴*Joseph Henry Laboratory, Department of Physics,*

Princeton University, Princeton, New Jersey 08544, USA

⁵*Department of Chemistry, Peking University, Beijing 100871, China*

⁶*College of Physics, Optoelectronics and Energy,*

Soochow University, Suzhou 215006, China

⁷*Institute of Physics, Academia Sinica, Taipei 11529, Taiwan*

[*] e-mail: gwljiahuang@pku.edu.cn

[†] These authors contributed equally to this work

Abstract

In the history of condensed matter physics, reinvestigation of a well-studied material with enhanced quality sometimes led to important scientific discoveries. A well-known example is the discovery of fractional quantum Hall effect in high quality GaAs/AlGaAs heterojunctions. Here we report the first single crystal growth and magnetoresistance (MR) measurements of the silver chalcogenide β -Ag₂Se (Naumannite), a compound has been known for the unusual, linear-field-dependent MR in its polycrystalline form for over a decade [1, 2]. With the quantum limit (QL) as low as 3 Tesla, a moderate field produced by a superconductor magnet available in many laboratories can easily drive the electrons in Ag₂Se to an unprecedented state. We observed significant negative longitudinal MR beyond the QL, which was understood as a ‘charge-pumping’ effect between the novel fermions with opposite chiralities. Characterization of the single-crystalline Ag₂Se and the fabrication of electric devices working above the QL, will represent a new direction for the study of these exotic electrons.

PACS numbers:

Electrons in metal move in the quantized orbits known as Landau levels (LLs) in an external magnetic field [3, 4]. The so-called quantum limit (QL) is attained when the magnetic field is higher than that corresponds to the lowest LL, in which all the electrons are confined in one highly degenerate state. Beyond the QL, the electrons are further fractionalized in two-dimensional (2D) electron gas, while little is known about the three-dimensional (3D) systems. Unfortunately very few materials manifest their electron concentration dilute enough so that the QL is accessible. Here we show that the single-crystalline β -Ag₂Se, a well-known quantum material, is one candidate for the exploration of this unknown region.

The mineral Naumannite (β -Ag₂Se) was first discovered in 1828. It crystallizes in a non-central-symmetric structure which has an orthorhombic unit cell ($P2_12_12_1$) with two crystallographic distinct silver atoms and one selenium atom [5, 6] (Fig. 1 insets). Previous studies showed that polycrystalline β -Ag₂Se manifested large, linear-field-dependent, transversal magnetoresistance (MR) at both low and high temperature regions [1, 7]. This linear MR remains unsaturated as a function of magnetic field strength up to 50 Tesla (T). It was believed that the origin of this unusual linear MR is either a quantum effect of electron correlation due to a linear dispersion at the energy where the conduction and valence bands cross [2, 8], or a classical effect of spatial conductivity fluctuations in strongly inhomogeneous polycrystals [9, 10]. Very recently topological characteristics of electrons in Ag₂Se due to spin orbital coupling (SOC) were emphasized [11].

Although various papers have been published on the studies of polycrystalline and nano-size Ag₂Se [12–14], research on a macro-size single crystal has never been reported until now. The difficulty of the single crystal growth comes from the thermal instability of the β -phase: it undergoes a first order, polymorphic structural transition to a cubic, high-temperature α -phase at 133° C. In the α -phase, selenium atoms form a body-centered cubic frame and silver atoms are distributed over several interstitial sites [15, 16]. During a regular crystal growth process, α -Ag₂Se intends to form a multi-domain polycrystalline β -phase when cooling to the room temperature. By contrast, we discovered a novel modified self-selecting vapour growth technique [17], which enables us to obtain single crystals of β -Ag₂Se above the transition temperature (See details in Method Part and Supplemental Information (SI)). During this growth process, the vapour from polycrystalline Ag₂Se condensed on small seed plates of the α -phase, leading to the ribbon-like β -phase single crystals (Fig. 1 inset). Macro-size single crystals of β -Ag₂Se exclusively provide a chance for studying the electronic states

via transport measurements with less influence of scattering from defects, particularly from the grain boundaries in polycrystals. We focus on the MR measurements for the current (I) along the crystallographic \mathbf{a} direction while the magnetic field can be along different directions in this paper (Fig. 1 inset).

Temperature dependent resistivity of single crystalline Ag_2Se shows a similar profile as that of previously reported in polycrystals [1, 7]: a broad maximum occurs around 100 K, below which the resistivity shows a metallic-like behavior (Fig. 1). The resistivity of the samples R1 and R2 that are from one growth batch shows one order of magnitude less than that of the samples R3 and R4 from the other. Hall measurements (for $I//\mathbf{a}$, $H//\mathbf{b}$, and Hall voltage along \mathbf{c}) reveal that all samples are n -type for the whole temperature range and the carrier density is $n = 4.9 \times 10^{19}\text{cm}^{-3}$ and $2.4 \times 10^{18}\text{cm}^{-3}$ for the samples R1 and R4 at 2 K, respectively (See SI and Table I). The n -type carriers most likely come from a small amount of deficiencies of selenium atoms commonly observed in selenide compounds [18]. Both R1 and R4 show mobility ($\mu_b = 1/\rho ne$) about $1000 \text{ cm}^2/(\text{V} \cdot \text{s})$ at 2 K, leading to a product of the classical cyclotron frequency to the scattering time, $\omega_C\tau = \mu_b B < 1$ at 9 T [3].

Figure 2 shows the MR (defined as $\Delta\rho_H/\rho_0$) of the samples R2 and R4 along the three principal axes at representative temperatures. The transversal MR for $H//\mathbf{b}$ and \mathbf{c} shows a similar profile: it crosses over from a quadratic dependence on H at low fields, to a linear and unsaturated dependence up to 9 T. This linear and unsaturated MR up to 300 K is similar to the previous reports in polycrystals [1, 7, 19]. For $H//\mathbf{b}$ in R1 and R2, weak Shubnikov-de Haas (SdH) oscillations occur on the linear background when $T < 10$ K and $\mu_0 H > 5$ T, but not in R3 and R4. Further analysis reveals that these single-frequency oscillations came from a relatively large Fermi extremal surface ($S_{F2} = 49$ T and 36 T for R1 and R2, respectively, see more details in SI). Given that these oscillations only appear in the samples with large carrier densities, we expect that they most likely come from a 3D electron band with a conventional energy dispersion. Further measurement in higher magnetic fields is prepared.

At first glance, the longitudinal magnetoresistance (LMR) of R2 and R4 for $H//\mathbf{a}$ shows different profiles at low temperatures: R2 shows strong SdH oscillations up to 9 T, while R4 shows weak oscillations when $H < 3.2$ T. Beyond this field corresponding to the lowest quantized LL, R4's LMR dramatically decreases with increasing H , *ie.*, R4 shows negative

LMR above the QL. The Lifshitz-Onsager rule is employed to understand the quantization of the Fermi surface cross-section area S_F as a function of the magnetic field B :

$$S_F \frac{\hbar}{eB} = 2\pi(n + \gamma) \quad (1)$$

where \hbar is the Planck's constant; e is the elementary charge; n is the LL index, and γ is the Onsager phase. The SdH oscillations of R2 originate from a small Fermi surface with $S_{F1} = 8.1$ T, and the peaks at ± 6.8 T correspond to $n = 1$ (See Fig.3 D and E). It is noteworthy that when $T = 40$ K, the oscillations fade out but the negative LMR still persists. On the other hand, the SdH oscillations in R4 originate from an even smaller Fermi surface with $S_{F1} = 3.8$ T, and a field larger than 3.2 T drives the system beyond the QL (See Fig.3 F and G). The oscillations fade out above 10 K, but the negative LMR persists until 25 K, and then it is dramatically suppressed to a very small, positive signal above 50 K. Although R1 and R3 have different S_F , their LMR manifests a similar behavior in rescaled H with respect to S_F : i), the negative LMR is always found to occur as long as the magnetic field is higher than the QL; ii), the negative LMR is not a part of oscillations since it survives at higher temperatures which destroy the oscillations. These phenomena described above have been observed in a dozen of samples with various sizes and n (see SI and Table I for the samples R1 and R3). Based on the analysis we believe that the negative LMR is due to a band effect above the QL. It is noteworthy that the LMR of R3 and R4 shows a shoulder-like anomaly around 6 T (indicated by the arrows in Fig. 2 and SI). These anomalies are located at the fields that are very close to the $n = 1/2$ in the LL indices (Fig. 4 C and E) for various samples with different S_F . It is likely due to the magnetic field induced spontaneous symmetry breaking which drives the system into a fractional filled LL. Further studies are needed to clarify this anomaly.

In order to address the Fermi surface topology and the nature of the electrons contributing to the SdH oscillations, we measured the MR while rotating the direction of the magnetic field with respect to the three principal axes at 2 K (Fig. 3 A, B, C and SI). When the direction of the field changes from **a** to **b** or to **c**, the MR of R2 shows a very similar profile with respect to the change of ϕ and ψ : the oscillations persist until ϕ and $\psi = 60^\circ$, while the negative MR is fully compensated by the linear contribution from the transversal MR for ϕ and $\psi > 30^\circ$. Figure 3 D and E show the resistivity (ρ_H) versus the reciprocal of the field component along the **a** direction for R2. The oscillations' period only depends on the

field component along the \mathbf{a} direction, whenever the field is tilted to \mathbf{b} or \mathbf{c} . A similar angle dependent behaviors for R4 is shown in Fig. 3 F, G and SI.

Based on the analysis of the SdH oscillations along different directions in R2, the frequencies are plotted as a function of the angles in Fig. 4 A and B. A clear $1/\cos\phi$ and $1/\cos\psi$ dependence up to 60° is observed on the Fermi surface S_{F1} , which indicates that the electrons are distributed highly two-dimensionally and S_{F1} has the geometry of a cylinder or a highly anisotropic ellipsoid. The LL indices for all four samples are shown in Fig.4 C. The resistivity associated with the SdH oscillations is expressed as [4, 20]:

$$\rho_H = \rho_0[1 + A(B, T)\cos 2\pi(S_F/B + \gamma)], \quad (2)$$

where

$$A(B, T) \propto \exp(-2\pi^2 k_B T_D / \hbar \omega_C) \cdot \frac{2\pi^2 k_B T / \hbar \omega_C}{\sinh(2\pi^2 k_B T / \hbar \omega_C)}. \quad (3)$$

In Eq. 3, T_D is the Dingle temperature; k_B is the Boltzmann's constant; and the cyclotron frequency $\omega_C = eB/m^*$. Based on Eq. 2, the peak and valley positions of ρ_{zz} are indicated as integer and half-integer, respectively. The interpolations of the lines n versus $1/\mu_0 H$ for all four samples show that the intercepts are clustered around $\gamma = -0.15 \pm 0.05$, although S_{F1} varies from 13.3 T to 3.8 T. This near-to-zero phase shift indicates a non-trivial Berry phase associated with Dirac or Weyl fermions [21, 22]. The effective mass ($m^* = eB/\omega_C$) was obtained from the temperature dependence of the peak amplitude at $n = 1$ for R2 and R4, yielding 0.075 and 0.064 m_e , respectively (Fig.4 D). Other parameters including the Fermi wave vector ($k_F = \sqrt{\frac{2eS_F}{\hbar}}$), the Fermi velocity ($v_F = \hbar k_F / m^*$) and the Fermi energy ($E_F = v_F^2 m^*$) are listed in Table I. These results, together with the Hall effect measurements, are consistent with the picture in which the Fermi levels of R3 and R4 lay at lower positions than those of R1 and R2 in a linearly dispersive electron band.

According to our measurements on various samples, we believe that the negative LMR is not a current jetting effect due to highly anisotropic or inhomogeneous conductance [3, 23] or improper contacts' positions (see more details in SI), nor a weak anti-localization effect of impurity scattering which is usually observed in 2DEG in low magnetic fields [24]. Under the condition of $\mu_b B < 1$, the classical scattering effect generally changes little with respect to the magnetic field [3]. The strong temperature dependence and the correlation with the QL indicate that such $> 20\%$ negative LMR must be caused by the band effect of Dirac fermions. Recently a weaker negative LMR was observed in Bi-Sb alloy with no indication

of SdH oscillations [25]. Besides that, negative LMR has never been reported in other Dirac electron systems such as Bi and Cd_3As_2 [26–29].

The crystal structure of $\beta\text{-Ag}_2\text{Se}$ differs from the other Dirac semimetals due to the absence of the central symmetry, which can lead to symmetry protected Weyl nodes induced by SOC [30]. In order to understand the chirality of electrons in Ag_2Se , we analyzed the low-energy effective Hamiltonian from the space group $\text{P}2_12_12_1$. In the absence of SOC, the single group of $\text{P}2_12_12_1$ for the spinless system possesses one-dimensional representation along $\Gamma\text{-X}$ (Σ) and $\Gamma\text{-Y}$ (Δ) axes in the Brillouin zone (BZ) [31]. The band structure possesses two Dirac-like bands around E_F on the high-symmetric Σ and Δ lines, respectively (Fig. 5 A). This result is consistent with the primary band structure calculation based on the density functional formalism (See SI). The bands hybridize each other and open gaps on the Σ and Δ lines in the presence of SOC (Fig. 5 B). One Dirac point at a high-symmetry line (Σ or Δ) splits to two Weyl points at different quadrants of the $k_x - k_y$ plane. The 3D Weyl Hamiltonian near E_F characterizes the band dispersion and the spin texture in vicinity of the gapless point $\mathbf{k}_0 = (k_{x0}, k_{y0}, 0)$ (Fig. 5 B). The other Weyl point near the Δ line in this quadrant has a higher energy and stays far from E_F . The two half-way screw operations of the Weyl point at \mathbf{k}_0 yield two opposite chiral Weyl points at $(-k_{x0}, k_{y0}, 0)$ and $(k_{x0}, -k_{y0}, 0)$, while a time reversal operation gives the Weyl point with identical chirality at $-\mathbf{k}_0$ (see Fig. 5 C).

The strong SdH oscillations with a large anisotropy in Ag_2Se indicate a large LL spacing when $H//\mathbf{a}$ (See SI). Above the QL, the electrons in a Weyl system entirely occupy the zeroth LL and only possess a momentum dispersion parallel to H [32, 33]. Such a chiral anomaly pumps electrons between Weyl points with the opposite chiralities at a rate proportional to the scalar product of the electric and the magnetic field $\vec{E} \cdot \vec{B}$, giving rise to a negative LMR along the direction that connects the pair of Weyl points [34, 35]. According to our calculations, the LLs from opposite Weyl points in Ag_2Se coexist around the projection point $\pm k_0$ when $H//\mathbf{a}$ (Fig. 5 D, see SI for details). Above the QL, the magnetic field further gives rise to a 2δ shift along the direction of the field due to a dynamical chiral shift induced by the electron-electron interactions (Fig. 5 D) [36]. The large momentum mismatch between the Fermi points in the zeroth LL impedes the backscattering process. Because the density of states is proportional to the magnetic field in the zeroth LL in an one dimensional momentum space, the longitudinal magneto-conductance ($\sigma = 1/\rho_{zz}$) increases

TABLE I: Parameters in samples R1 to R4. S_{F1} , k_{F1} and S_{F2} , k_{F2} are determined from the SdH periods on **a** direction and **b** directions, respectively. E_F and v_F are obtained from the T dependent amplitude of oscillations on a direction. Dash entries mean quantities not measured. N/A means quantities not observed.

| | n | S_{F1} | k_{F1} | γ | m^* | E_F | v_F | S_{F2} | k_{F2} |
|----|----------------------|----------|-------------------|------------------|-------|-------|------------------------|----------|-------------------|
| | cm^{-3} | T | \AA^{-1} | | m_e | meV | 10^5 ms^{-1} | T | \AA^{-1} |
| R1 | 4.9×10^{19} | 13.3 | 0.02 | -0.14 ± 0.04 | 0.1 | 30 | 2.3 | 49 | 0.039 |
| R2 | – | 8.1 | 0.016 | -0.18 ± 0.07 | 0.075 | 27 | 2.5 | 36 | 0.033 |
| R3 | – | 4.7 | 0.012 | -0.17 ± 0.01 | – | – | – | N/A | N/A |
| R4 | 2.4×10^{18} | 3.8 | 0.011 | -0.18 ± 0.01 | 0.064 | 18 | 2.2 | N/A | N/A |

linearly with $\mu_0 H$ above the QL (Fig. 4 E). This linear positive magneto-conductance in Ag_2Se is not like an H^2 dependence due to the impurity scattering effect [37], but more like a characteristic of anomalous transport properties for a Weyl semimetal [32, 34].

In summary, we synthesized macro-size single crystals of β -phase Ag_2Se and measured their resistance in magnetic fields. While the linear transversal MR was confirmed, the LMR showed strong SdH oscillations and a large, negative component beyond the QL. This anomalous MR was understood as an electron pumping effect induced by chiral anomaly in the zeroth LL. Our measurements also indicated that the negative LMR will be saturated at the base temperature when the magnetic field is far beyond the QL. Some first-step measurements hinted that the sample will become an insulator in a sufficiently high magnetic field. Finally, we infer that the vapour transfer growth method bears more efforts for synthesizing the single crystals of new materials, especially for the thermally unstable compounds.

Methods

Polycrystalline β - Ag_2Se was prepared from stoichiometric Ag and Se in a sealed quartz tube at 800°C for two days. The yield was then ground and sealed in a long quartz ampoule in vacuum, and placed in a tube furnace with temperature gradient from 500°C to a temperature close to the room temperature for 7 days. The single crystals yielded are ribbon-like and their sizes range from $20\mu\text{m} \times 20\mu\text{m} \times 2\text{mm}$ to $0.5\text{mm} \times 0.5\text{mm} \times 10\text{mm}$

(Fig. 1 inset). The details of the crystal growth are discussed in SI part. Single-crystal X-ray diffraction data was collected on a Agilent SuperNova diffractometer with a micro-focus Mo source ($\lambda = 0.7107\text{\AA}$). The data reduction was precessed by the CrysAlis Pro package. Multi-scan absorption correction was applied. All physical property characterizations were performed on a Quantum Design Physical Property Measurement System (PPMS-9) . The first-principles calculations are based on the generalized gradient approximation (GGA) [38] using the full-potential projected augmented wave method [39, 40] as implemented in the VASP package [41–43]. Electronic structure calculations were performed over $12 \times 6 \times 6$ Monkhorst-Pack k -mesh included self-consistently.

Acknowledgments

The authors thank Jun Xiong, Fang Chen and Fa Wang for helpful discussion, and Kaihui Liu for assistance with TEM measurements. The authors thank Jian Wang and Yuan Li for using their instruments as well. S. Jia is supported by National Basic Research Program of China (Grant Nos. 2013CB921901 and 2014CB239302). X. C. Xie is supported by NBRPC (Grant Nos. 2012CB821402 and 2015CB921102) and NSFC under Grant No. 91221302. J. L. Sun is supported by NSFC under Grant No. 91222107. SYX and MZH are supported by U.S. DOE DE-FG-02-05ER46200 TRC and HTJ are supported by the National Science Council and Academia Sinica, Taiwan. We also thank NCHC, CINC-NTU, and NCTS, Taiwan for technical support.

-
- [1] R. Xu, A. Husmann, T. F. Rosenbaum, M.-L. Saboungi, J. E. Enderby, and P. B. Littlewood. Large magnetoresistance in non-magnetic silver chalcogenides. *Nature*, 390(6655):57–60, nov 1997.
 - [2] A. A. Abrikosov. Quantum magnetoresistance. *Phys. Rev. B*, 58:2788–2794, Aug 1998.
 - [3] Alfred Brian Pippard. *Magnetoresistance in Metals*. Cambridge University Press, 2009.
 - [4] D. Shoenberg. *Magnetic oscillations in metal*. Cambridge University Press, 2009.
 - [5] G. A. Wieggers. The crystal structure of the low-temperature form of silver selenide. *American mineralogist*, 56:1882, 1971.

- [6] Heinrich Billetter and Uwe Ruschewitz. Structural phase transitions in Ag_2Se (naumannite). *Zeitschrift für anorganische und allgemeine Chemie*, 634(2):241–246, 2008.
- [7] A. Husmann, J. B. Betts, G. S. Boebinger, A. Migliori, T. F. Rosenbaum, and M.-L. Saboungi. Megagauss sensors. *Nature*, 417(6887):421–424, may 2002.
- [8] A. A. Abrikosov. Quantum linear magnetoresistance. *EPL (Europhysics Letters)*, 49(6):789, 2000.
- [9] M. M. Parish and P. B. Littlewood. Non-saturating magnetoresistance in heavily disordered semiconductors. *Nature*, 426(6963):162–165, nov 2003.
- [10] Jingshi Hu and T. F. Rosenbaum. Classical and quantum routes to linear magnetoresistance. *Nat Mater*, 7(9):697–700, sep 2008.
- [11] Wei Zhang, Rui Yu, Wanxiang Feng, Yugui Yao, Hongming Weng, Xi Dai, and Zhong Fang. Topological aspect and quantum magnetoresistance of $\beta\text{-Ag}_2\text{Te}$. *Phys. Rev. Lett.*, 106:156808, Apr 2011.
- [12] Zhao Zhao, Shibing Wang, Artem R. Oganov, Pengcheng Chen, Zhenxian Liu, and Wendy L. Mao. Tuning the crystal structure and electronic states of Ag_2Se : Structural transitions and metallization under pressure. *Phys. Rev. B*, 89:180102, May 2014.
- [13] Byron Gates, Yiyang Wu, Yadong Yin, Peidong Yang, and Younan Xia. Single-crystalline nanowires of Ag_2Se can be synthesized by templating against nanowires of trigonal Se. *Journal of the American Chemical Society*, 123(46):11500–11501, 2001.
- [14] Jaemin Yu and Hoseop Yun. Reinvestigation of the low-temperature form of Ag_2Se (naumannite) based on single-crystal data. *Acta Crystallographica Section E*, 67(9):i45, Sep 2011.
- [15] P. Rahlfs. The cubic high temperature modifiers of sulfides, selenides and tellurides of silver and of uni-valent copper. *Z. Phys. Chem*, B 31:157, 1936.
- [16] Y. Kumashiro, T. Ohachi, and I. Taniguchi. Phase transition and cluster formation in silver selenide. *Solid State Ionics*, 86C88, Part 2(0):761 – 766, 1996. Proceedings of the 10th International Conference on Solid State Ionics.
- [17] Andrzej Szczerbakow and Ken Durose. Self-selecting vapour growth of bulk crystals - principles and applicability. *Progress in Crystal Growth and Characterization of Materials*, 51(1C3):81 – 108, 2005.
- [18] Shuang Jia, Huiwen Ji, E. Climent-Pascual, M. K. Fuccillo, M. E. Charles, Jun Xiong, N. P. Ong, and R. J. Cava. Low-carrier-concentration crystals of the topological insulator $\text{Bi}_2\text{Te}_2\text{Se}$.

- Phys. Rev. B*, 84:235206, Dec 2011.
- [19] Z. Ogorelec, A. Hamzić, and M. Basletić. On the optimization of the large magnetoresistance of Ag_2Se . *EPL (Europhysics Letters)*, 46(1):56, 1999.
- [20] G. Landwehr and E. I. Rashba. *Landau Level spectroscopy*, volume 27.2. North-Holland, Amsterdam, 1991.
- [21] G. P. Mikitik and Yu. V. Sharlai. Berry phase and the phase of the shubnikov-de haas oscillations in three-dimensional topological insulators. *Phys. Rev. B*, 85:033301, Jan 2012.
- [22] H. Murakawa, M. S. Bahramy, M. Tokunaga, Y. Kohama, C. Bell, Y. Kaneko, N. Nagaosa, H. Y. Hwang, and Y. Tokura. Detection of berrys phase in a bulk rashba semiconductor. *Science*, 342(6165):1490–1493, 2013.
- [23] Jingshi Hu, T. F. Rosenbaum, and J. B. Betts. Current jets, disorder, and linear magnetoresistance in the silver chalcogenides. *Phys. Rev. Lett.*, 95:186603, Oct 2005.
- [24] D. J. Bishop, R. C. Dynes, and D. C. Tsui. Magnetoresistance in si metal-oxide-semiconductor field-effect transistors: Evidence of weak localization and correlation. *Phys. Rev. B*, 26:773–779, Jul 1982.
- [25] Heon-Jung Kim, Ki-Seok Kim, J.-F. Wang, M. Sasaki, N. Satoh, A. Ohnishi, M. Kitaura, M. Yang, and L. Li. Dirac versus Weyl Fermions in Topological Insulators: Adler-Bell-Jackiw Anomaly in Transport Phenomena. *Phys. Rev. Lett.*, 111:246603, Dec 2013.
- [26] Sei-ichi Tanuma and Rumiko Inada. Magneto-phonon effect in the longitudinal magnetoresistance of bismuth. *Progress of Theoretical Physics Supplement*, 57:231–241, 1975.
- [27] Benoît Fauqué, Baptiste Vignolle, Cyril Proust, Jean-Paul Issi, and Kamran Behnia. Electronic instability in bismuth far beyond the quantum limit. *New Journal of Physics*, 11(11):113012, 2009.
- [28] P. Dziawa, B. J. Kowalski, K. Dybko, R. Buczko, A. Szczerbakow, M. Szot, E. Łusakowska, T. Balasubramanian, B. M. Wojek, M. H. Berntsen, O. Tjernberg, and T. Story. Topological crystalline insulator states in $\text{Pb}_{1-x}\text{Sn}_x\text{Se}$. *Nat Mater*, 11(12):1023–1027, dec 2012.
- [29] Tian Liang, Quinn Gibson, Mazhar N. Ali, Minhao Liu, R. J. Cava, and N. P. Ong. Ultrahigh mobility and giant magnetoresistance in the dirac semimetal Cd_3As_2 . *Nat Mater*, advance online publication, nov 2014.
- [30] Shuichi Murakami. Phase transition between the quantum spin hall and insulator phases in 3d: emergence of a topological gapless phase. *New Journal of Physics*, 9(9):356, 2007.

- [31] Christopher John Bradley and Arthur P Cracknell. *The mathematical theory of symmetry in solids: representation theory for point groups and space groups*, volume 10. AMC press, 2010.
- [32] D. T. Son and B. Z. Spivak. Chiral anomaly and classical negative magnetoresistance of Weyl metals. *Phys. Rev. B*, 88:104412, Sep 2013.
- [33] Kai-Yu Yang, Yuan-Ming Lu, and Ying Ran. Quantum hall effects in a weyl semimetal: Possible application in pyrochlore iridates. *Phys. Rev. B*, 84:075129, Aug 2011.
- [34] Holger Bech Nielsen and Masao Ninomiya. The Adler-Bell-Jackiw anomaly and Weyl fermions in a crystal. *Physics Letters B*, 130(6):389–396, 1983.
- [35] Vivek Aji. Adler-Bell-Jackiw anomaly in Weyl semimetals: Application to pyrochlore iridates. *Phys. Rev. B*, 85:241101, Jun 2012.
- [36] E. V. Gorbar, V. A. Miransky, and I. A. Shovkovy. Engineering Weyl nodes in Dirac semimetals by a magnetic field. *Phys. Rev. B*, 88:165105, Oct 2013.
- [37] Petros N. Argyres. Galvanomagnetic effects in the quantum limit. *Journal of Physics and Chemistry of Solids*, 8(0):124 – 130, 1959.
- [38] John Perdew, Kieron Burke, and Matthias Ernzerhof. Generalized gradient approximation made simple. *Phys. Rev. Lett.*, 77:3865–3868, Oct 1996.
- [39] P. Blöchl. Projector augmented-wave method. *Phys. Rev. B*, 50:17953–17979, Dec 1994.
- [40] G. Kresse and D. Joubert. From ultrasoft pseudopotentials to the projector augmented-wave method. *Phys. Rev. B*, 59:1758–1775, Jan 1999.
- [41] G. Kresse and J. Hafner. *Ab initio* molecular dynamics for open-shell transition metals. *Phys. Rev. B*, 48:13115–13118, Nov 1993.
- [42] G. Kresse and J. Furthmüller. Efficient iterative schemes for *ab initio* total-energy calculations using a plane-wave basis set. *Phys. Rev. B*, 54:11169–11186, Oct 1996.
- [43] G. Kresse and J. Furthmüller. Efficiency of ab-initio total energy calculations for metals and semiconductors using a plane-wave basis set. *Computational Materials Science*, 6(1):15 – 50, 1996.

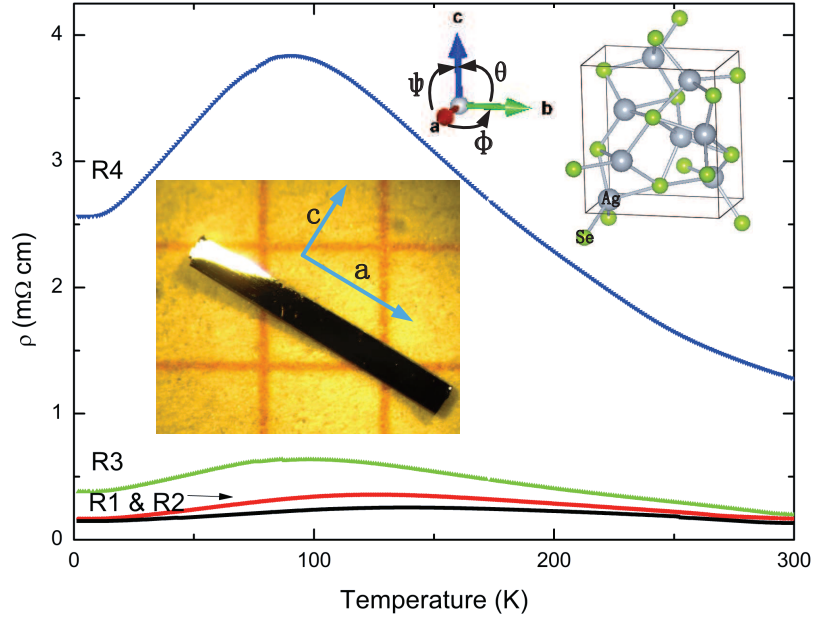


FIG. 1: **Temperature dependent resistivity of single crystalline β -Ag₂Se.** The resistivity along **a** direction is similar as previously reported polycrystalline samples with similar carrier density n . Upper inset: the unit cell and the definition of angles θ , ϕ and ψ among three principal axes. Central inset: an image of a crystal under microscope. The scale is 1×1 mm.

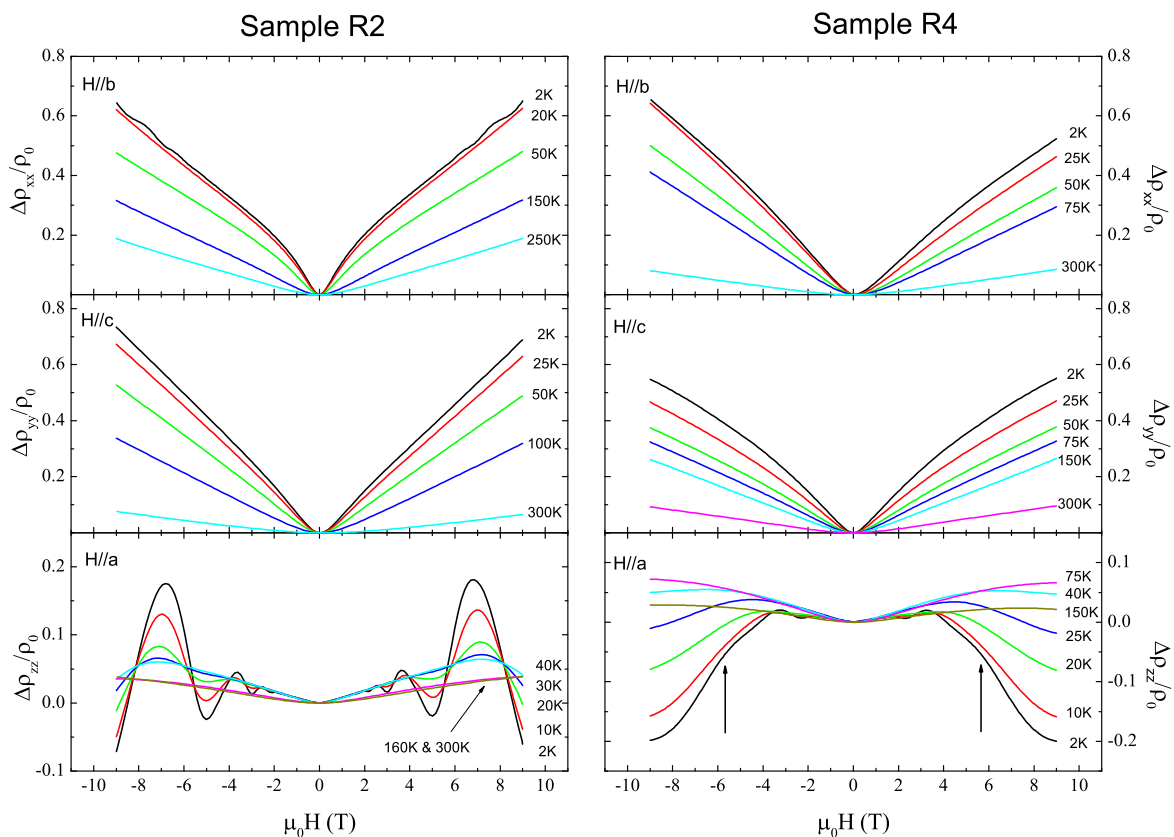


FIG. 2: MR ($\Delta\rho/\rho_0$) for the samples R2 and R4 along three principal axes at representative temperatures. $\Delta\rho_{xx}$, $\Delta\rho_{yy}$ and $\Delta\rho_{zz}$ are for $H//\mathbf{b}$, \mathbf{c} and \mathbf{a} , respectively. Since the raw data are highly symmetric, the treatment of $\rho_H = (\rho_{+H} + \rho_{-H})/2$ was not applied. The arrows in the lower right panel show the shoulder-like anomaly above the QL.

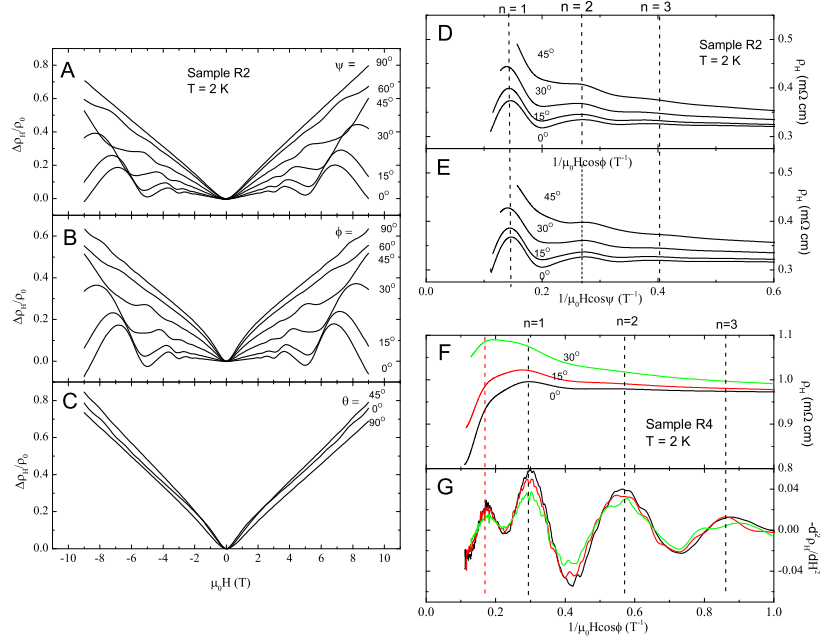


FIG. 3: **Anisotropy of MR for the samples R2 and R4 at 2 K.** Panel A, B and C: the MR for R2 when the direction of the field change among three principal axes at 2 K. No symmetry treatment of $\pm H$ was applied. The MR slightly changes when θ changes from 0° to 90° . Panel D and E: the resistivity versus $1/\mu_0 H_a = 1/(\mu_0 H \cos\phi)$ and $1/(\mu_0 H \cos\psi)$ for R2 at 2 K, respectively. Panel F and G: ρ_H and $-d^2\rho_H/dH^2$ versus $1/\mu_0 H_a = 1/(\mu_0 H \cos\phi)$ for R4 at 2 K. The red dashed line on the left represents the position of the shoulder-like anomaly beyond the QL (see more details in the main text).

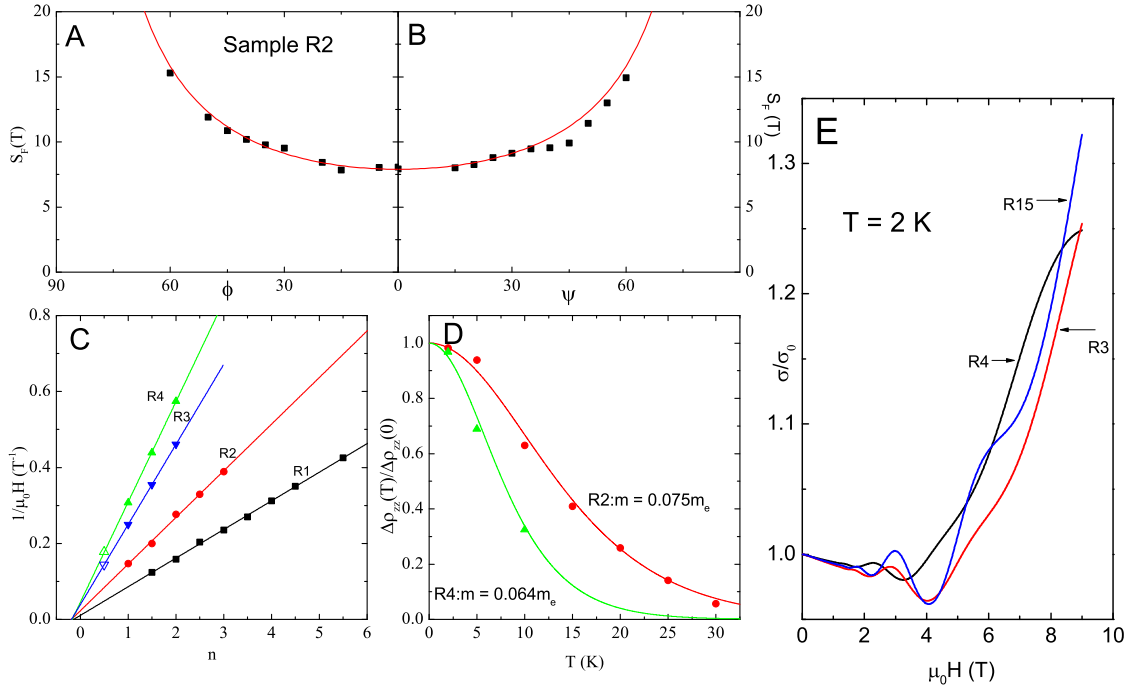


FIG. 4: **Analysis of SdH oscillations and negative LMR in Ag_2Se .** Panel A and B: S_{F1} for R2 varying with ϕ and ψ as $1/\cos\phi$ and $1/\cos\psi$ (red curve), respectively. Panel C: Landau level indice for all 4 samples. Two open symbols present the anomaly at $n = 1/2$ for R3 and R4. Panel D: Temperature dependence of the SdH oscillations amplitude at $n = 1$ for R2 and R4. Panel E: magneto-conductance for three samples showing negative LMR below 9 T at 2 K. The arrows indicate that a linear magneto-conductance occurs when the field is higher than the position of the shoulder-like anomaly.

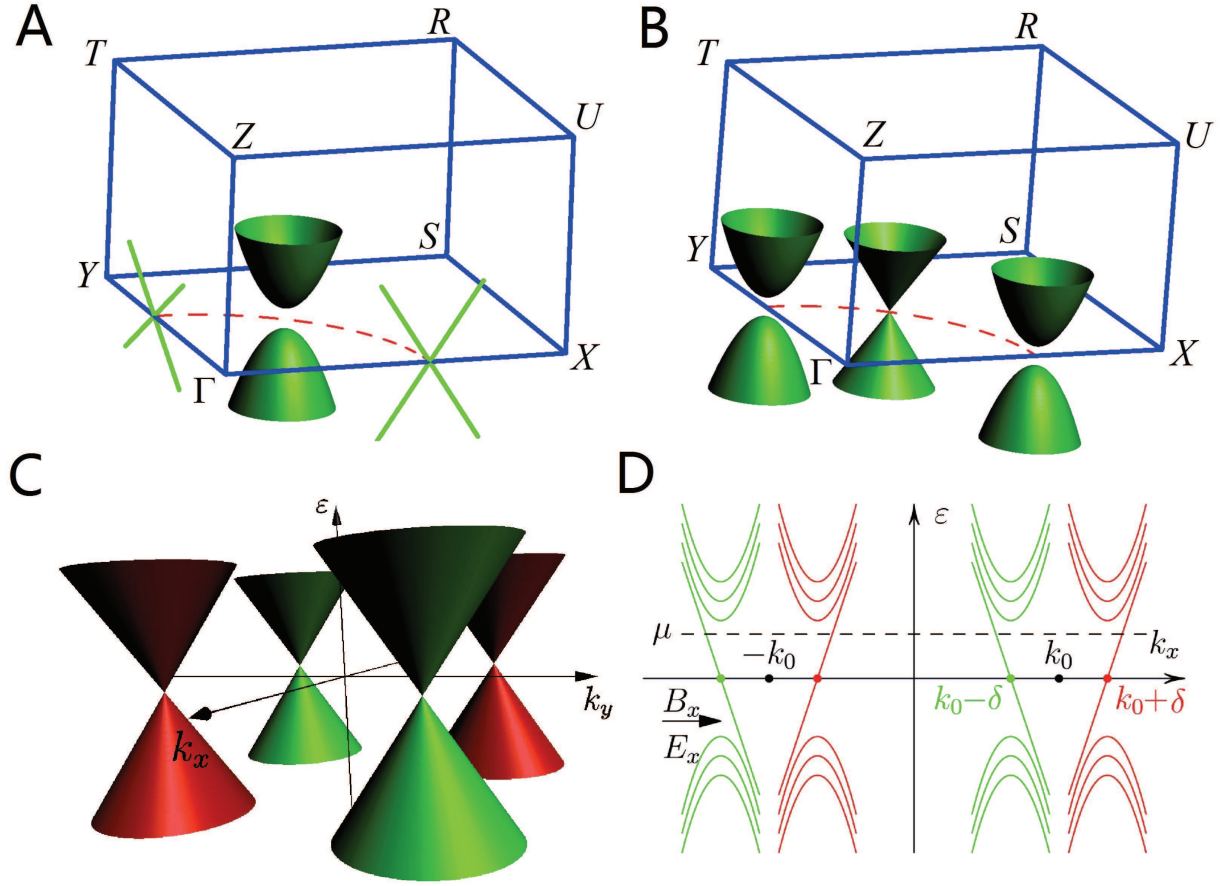


FIG. 5: Schematic plots of energy bands of Ag_2Se . Panel A and B: The energy bands for spinless and spinful system, respectively. Panel C: Weyl nodes in the BZ. Panel D: Landau levels for $B \parallel X$ when the dynamical chiral shift 2δ is counted.